POLYTECHNIQUE MONTRÉAL

affiliée à l'Université de Montréal

Novel Raman spectroscopy fiber optics system design can enable intraoperative tissue probing for focal cortical dysplasia in children

HUGO LE MOEL

Institut de génie biomédical

Mémoire présenté en vue de l'obtention du diplôme de *Maîtrise ès sciences appliquées*

Génie biomédical

Mars 2025

POLYTECHNIQUE MONTRÉAL

affiliée à l'Université de Montréal

Ce mémoire intitulé :

Novel Raman spectroscopy fiber optics system design can enable intraoperative tissue probing for focal cortical dysplasia in children

présenté par **Hugo LE MOEL**

en vue de l'obtention du diplôme de *Maîtrise ès sciences appliquées*

a été dûment accepté par le jury d'examen constitué de :

Thomas GERVAIS, président

Frédéric LEBLOND, membre et directeur de recherche

Stephan REUTER, membre

DEDICATION

To my biological and chosen families,

To my cat Maddie who I love dearly,

To Selene….

ACKNOWLEDGEMENTS

I would like to first thank deeply my professor Frédéric Leblond who saw potential in me and gave me a chance to express it. I would also like to thank Trang who supported me in the laboratory all those years. Guillaume and Fredo, I will never be able to thank you enough for your infinite patience and the time you both took answering my innocently very complex questions and help me with my programming codes. Billie, Esmat, Sandryne and all the others you made my passage into the laboratory a core memory of mine. I'll cherish those instants for a long time.

This last year was probably one of the most difficult of my life and I would not have made it will all those people. Claire, Charlie, Camille, Stella, Mika, Matt, Artémis, Béatrice, Yuki, Alice, Solène, Florence, Amanda, Stella, Mare, Marilou, Gen, Ariel, Vi and Thomas, I am more than glad to be your friend and think of all of you as family.

At last, I would like to thank *Hugo* who never gave up and always stayed curious despite hating himself. I am deeply sorry for not achieving your PhD dream and am so grateful for you allowing me to be who I am today.

RÉSUMÉ

Cette thèse de maîtrise explore l'intégration clinique d'un système innovant de spectroscopie Raman portatif à sonde ponctuelle comme outil chirurgical *in situ* pour la détection de la dysplasie corticale focale (FCD) dans le cortex de patients pédiatriques. La FCD est la principale cause d'épilepsie réfractaire chez l'enfant, et la chirurgie constitue le traitement le plus courant. Cependant, même avec les techniques les plus avancées, le taux de succès de ces interventions reste inférieur à 60 %. L'essor de la spectroscopie Raman en tant qu'outil chirurgical ces dernières années représente une opportunité prometteuse pour améliorer les chances de rémission totale des crises chez ces patients.

Dans cette étude, deux systèmes spectroscopie Raman ont été systématiquement comparés en utilisant des échantillons d'acquisition identiques. Les résultats montrent que le système le plus récent permet d'acquérir des spectres en un temps dix fois inférieur à celui du système précédemment utilisé, tout en maintenant un rapport signal/bruit et une qualité spectrale équivalents.

Ce nouveau système a été intégré avec succès dans le flux de travail clinique de deux blocs opératoires à Montréal. Au cours des deux dernières années, 169 acquisitions Raman ont été collectées auprès de 23 patients. Néanmoins, compte tenu de la qualité actuelle des données actuelles, un ensemble de données composé d'au moins 350 acquisitions Raman serait nécessaire pour obtenir une différence statistiquement significative entre les tissus FCD et les tissus cérébraux normaux. Malgré cette limitation, une référence pour les futurs algorithmes de classification a été établie, visant une sensibilité de 70 % et une spécificité de 64 %.

Les récentes améliorations logicielles et matérielles au sein du laboratoire de recherche, ainsi qu'une augmentation constatée de la qualité des mesures lors des derniers cas cliniques, renforcent la confiance quant à la réussite future de cette étude.

ABSTRACT

This master's thesis explores the clinical integration of a novel handheld Raman point probe spectroscopy system as an in-situ surgical tool for detecting focal cortical dysplasia (FCD) in the cortex of pediatric patients. FCD is the leading cause of drug-resistant epilepsy in children, with surgical intervention being the most common treatment. However, even with the most advanced techniques, the success rate of these procedures remains below 60%. The emergence of Raman spectroscopy as a surgical tool in recent years presents a promising opportunity to improve the likelihood of achieving seizure freedom for these patients.

In this study, two handheld Raman point probe systems were systematically compared using identical acquisition samples. The results showed that the newer system is capable of acquiring spectra in one-tenth of the time required by the currently available system while maintaining an equivalent signal-to-noise ratio and overall spectral quality.

The novel system was successfully integrated into the clinical workflow of two operating rooms in Montréal. Over the past two years, 169 Raman acquisitions have been collected from 23 patients. However, based on the current data quality, a minimum of 350 total Raman acquisitions would be required to achieve statistically significant differences between FCD and normal brain tissue. Despite this limitation, a benchmark for future classification algorithms was established, targeting a sensitivity of 70% and a specificity of 64%.

Recent software and hardware improvements within the research laboratory, along with an observed increase in measurement quality in the latest clinical cases, provide strong confidence in the future success of this study.

TABLE OF CONTENTS

LIST OF TABLES

LIST OF FIGURES

LISTE OF SYMBOLS AND ABBREVIATIONS

FCD ……..…… Focal cortical dysplasia

MDRD ……..… Medical device reprocessing department

OR ……..….. Operating room

ILAE ……..... International league against epilepsy

MRI …….. Magnetic resonance imaging

FDG-PET ……. Fluorodeoxyglucose positron emission tomography

SPECT …….. Single photon emission computed tomography

EEG …….. Electroencephalography

ECoG …… Electrocorticography

SEEG …… Stereoelectroencephalography

MEG ……. Magnetoencephalography

NIR ……... Near infrared

NAD(P)H ……. Nicotinamide adenine dinucleotide

FAD ……. Flavin adenine dinucleotide

SNR ……. Signal to noise ratio

CCD ….…… Charged couple device

QF …… Quality factor

SNV…….. Standard normal variate

TP …… True positive

TN …… True negative

FP ……. False positive

FN …… False negative

ROC ……. Receiver operating characteristic

FPR …….. False positive rate

TPR …….. True positive rate

CHAPTER 1 INTRODUCTION

1.1 Context

Focal cortical dysplasia (FCD) is a developmental malformation of the cerebral cortex that occurs during the prenatal stages of brain development. This abnormality is widely recognized as one of the leading causes of drug-resistant epilepsy, which poses significant challenges for effective treatment. Currently, the primary treatment option for FCD involves surgically removing the malformed area of the cortex. However, the detection and localization of FCD remain complex and problematic, as the modern methods used for its identification are often imprecise and can be physically and emotionally taxing for patients. These limitations highlight the urgent need for innovative technologies capable of accurately detecting FCD tissue, thereby improving surgical outcomes and supporting existing detection and treatment methods.

Previous studies done in the laboratory have shown that Raman spectroscopy is effective for the *in vivo* detection of brain tumors, offering high sensitivity and specificity in distinguishing between healthy and diseased tissues (Lemoine, et al., 2019; Ember, et al., 2024; Leblond, et al., 2025). Moreover, a recent study to be published has indicated that Raman spectroscopy is also effective in detecting FCD tissues *ex vivo* (Trang, Leblond, Dallaire, Cayrol, & Dudley, in press). These findings suggest that technology has a strong potential to extend its application to the real-time identification of FCD tissue during surgical procedures.

In addition to its proven capabilities, recent advancements in optical technologies used in spectrometers and handheld Raman single-point probes could further enhance the application of this technique. These technological improvements may allow for the development of tools capable of providing real-time diagnoses of FCD during surgical interventions. Such advancements would significantly reduce the uncertainty associated with current detection methods and could lead to better surgical outcomes for patients with drug-resistant epilepsy. By integrating Raman spectroscopy with existing technologies, it may be possible to create a more precise, efficient, and patient-friendly approach to the diagnosis and treatment of FCD.

1.2 Hypotheses and objectives

This project has been carried out within the Lumed laboratory. The ultimate objective of this initiative is the development and deployment of the latest Raman spectroscopy single-point system across multiple hospitals. This cutting-edge system aims to assist surgeons in diagnosing focal cortical dysplasia (FCD) in real time during surgical procedures.

To guide the research and development process, two key hypotheses have been formulated for this project:

1.The enhancements made to the new Raman spectroscopy system will enable it to perform real-time measurements of FCD tissue during surgical interventions.

2.The improvements incorporated into the new Raman spectroscopy system will result in larger sensitivity and specificity for detecting FCD lesions compared to currently available imaging modalities.

Building upon the previously stated hypotheses, the following detailed goals have been established to guide the research project.

1. Characterization of the new system
    a. Develop a robust and standardized measurement protocol to facilitate a thorough comparison between the new Raman spectroscopy system and the previous systems employed in the laboratory.
    b. Conduct extensive data acquisition and processing for both the new and previous systems, following a standardized protocol developed in our laboratory.
2. Preparation and deployment of the system in clinical settings
    a. Work closely with the biomedical engineering departments of the selected clinical centers to implement necessary modifications to the system, ensuring compliance with institutional standards and guidelines.
    b. Collaborate with the Medical Device Reprocessing Department (MDRD) and the operating room (OR) team to coordinate the sterilization process of the Raman probe and its components.

c. Develop a comprehensive acquisition protocol in consultation with surgeons and nurses. This protocol will focus on ensuring the safety of all personnel, minimizing the impact of ambient OR lighting on Raman signal acquisition, and optimizing the workflow during surgical procedures.
d. Establish a secure and efficient method for sharing the Raman spectroscopy acquisition data and the corresponding pathological results with the entire clinical team.

3. Initiation of the clinical study at McGill and Sainte-Justine clinical centers
    a. Collaborate with the surgical teams at both institutions to identify and recruit suitable patients for the clinical study.
    b. For each surgical procedure, ensure the proper installation of the Raman spectroscopy system in the operating room. This includes placing the system near the patient in a manner that does not interfere with the surgical workflow and connecting the sterile probe securely to the system.
    c. During each measurement, validate with the surgeon the precise positioning of the Raman probe on the targeted tissue. To ensure optimal data quality, turn off all non-essential lights in the operating room and follow the established acquisition protocol to make the acquisition.
    d. For every measurement taken, meticulously document the resection label to enable accurate correlation with the corresponding pathological analysis.

1.3 Organisation of the document

The structure of the current document is organized into five chapters including the introduction. Following the introduction, the second chapter delves into a review of the existing literature related to FCD and Raman spectroscopy. This section provides a thorough examination of the characteristics of FCD, its impact on patients, and the limitations of current diagnostic methods. Additionally, it discusses Raman spectroscopy in detail, with particular attention to single-point handheld systems. The third chapter shifts focus to the technical aspects of the project, describing the modernization of the handheld probe and spectrometer that comprise the new Raman spectroscopy system. Building on this technical foundation, the fourth chapter explores the clinical

study associated with the project. It provides an account of the methodology, including patient recruitment, the setup of the system in operating rooms, and the acquisition of Raman spectra during surgeries. The document concludes with a final chapter that synthesizes the key results and evaluates their significance.

CHAPTER 2 REVIEW OF LITTERATURE

2.1 Focal cortical dysplasia

2.1.1 FCD classification (Najm, et al., 2022)

Focal cortical dysplasia is a malformation of cortical development. The International League Against Epilepsy (ILAE) updated their classification system for FCD, expanding it from three subtypes to five. This updated classification provides a more detailed understanding of the different types of FCD, making it easier for doctors and researchers to identify and study the specific characteristics of each type.

First class, FCDI, corresponds to malformations of the cortical layers structure. The ILAE has divided FCDI into three subclasses: FCDIa, FCDIb, and FCDIc. FCDIa is defined by an excessive number of cortical minicolumns. FCDIb involves a disruption of the horizontal cortical layers. FCDIc combines features of both FCDIa and FCDIb, as it includes abnormalities in both the horizontal and vertical layers of the cortex.

Second class, FCDII, corresponds to malformation of the neurons cells themselves. The ILAE has divided FCDII into two subclasses: FCDIIa and FCDIIb FCDIIa is characterized by the presence of dysmorphic neurons. These neurons are abnormally large and have irregular shapes compared to normal neurons. FCDIIb has all the features of FCDIIa but also includes balloon cells. FCDII is the most common form of malformation of cortical development.

The third class, FCDIII, describes malformations in the cortical layers that occur due to another condition or disease. The ILAE has identified four subclasses of FCDIII: FCDIIIa, FCDIIIb, FCDIIIc, and FCDIIId. FCDIIIa is associated with hippocampal sclerosis, also called mesial temporal sclerosis. This condition involves significant loss of neurons in the hippocampus. In addition to neuron loss, there is gliosis, a process where glial cells multiply abnormally. FCDIIIb occurs when cortical dyslamination is found near a brain tumor. The tumor disrupts the normal structure of the cortical layers, leading to the malformation. FCDIIIc is related to vascular malformations, such as abnormal blood vessels, which interfere with the development of the brain's cortex. FCDIIId is caused by lesions that occur early in life. These early-acquired lesions can alter the normal development of the brain’s cortex, leading to dysplasia.

The fourth class of FCD was added in the 2022 ILAE update. This new class focuses on mild malformations of cortical development that occur in the white matter of the brain. This class is divided into two subclasses. The first subclass is characterized by an excessive presence of heterotopic neurons cells in the white matter. Heterotopic cells are cells present in an anomalous location. The second one is defined by an excessive density of oligodendroglia cells and heterotopic neurons in the white matter. Oligodendroglial cells are responsible for forming the myelin sheath, which surrounds and protects nerve fibers in the central nervous system.

The fifth and final class of FCD is used when no clear or specific FCD can be identified through histopathological examination. This class is referred to as "no definite FCD on histopathology." It applies to cases where the abnormalities are ambiguous, and a definitive diagnosis cannot be made.

2.1.2 FCD challenges

FCD is a severe condition that causes epilepsy, sometimes leading to a high number of seizures, with some patients experiencing as many as 100 seizures per day (Shakhatreh, et al., 2022). This makes the disease highly impairing for those who suffer from it. Furthermore, around 30% of people with this malformation cannot be treated effectively with medication (Spitzer, et al., 2022). This lack of response to antiepileptic drugs classifies their epilepsy as refractory or drug-resistant.

When seizures cannot be controlled with medications, surgery may become the only option for these patients. However, surgery is not a simple or straightforward solution. Before performing the surgery, surgeons must first create a detailed map of the patient’s brain to locate the epileptogenic zones as accurately as possible. This process involves advanced neuroimaging and neurophysiological methods (Yao, et al., 2024).

Magnetic resonance imaging (MRI) is the principal neuroimaging technology used for detecting epileptogenic zones (Guerrini & Barba, 2021). For some lesions, they can’t be detected by conventional MRI thus making the patients associated MRI-negative (Yao, et al., 2024). Fortunately for those patients, Fluorodeoxyglucose positron emission tomography (FDG-PET) is highly sensitive to FCD patients, and particularly those MRI-negative. However, the delineation of the epileptogenic zones is limited (Yao, et al., 2024). Coregistration of the MRI and FDG-PET images can help enhance the detection of seizure onset zones (Jayalakshmi S, 2019). For complex

cases where MRI and FDG-PET both fail to identify the epileptogenic zone, ictal single-photon emission computed tomography (SPECT) can be used. However, this technique tends to detect seizure propagations and make the epileptogenic zone appear bigger than it is (Guerrini & Barba, 2021).

In addition to neuroimaging techniques, neurophysiological ones are often used. Those techniques are used to record interictal and seizure onset electrical patterns from the brain. Scalp electroencephalography (EEG) isn't as effective for FCD-I as for FCD-II. However, this technique may give a signal correlated with the spatial location of the lesion (Shakhatreh, et al., 2022). Electrocorticography (ECoG) and stereoelectroencephalography (SEEG) are not very specific but their signals are quite sensitive to FCD-II. Intracranial EEG is proven to be at least as useful as its scalp counterpart. Additionally, some studies start to show that high frequency oscillations found with intracranial EEG could be used as epileptogenic activity marker of the lesion (Guerrini & Barba, 2021). Magnetoencephalography (MEG) has the advantage of being relatively insensitive of skull conductivity. This technique is highly sensitive but lowly specific to epileptic zones (Neugebauer F, 2022).

These procedures are essential but can be very challenging and exhausting for the patient. Each test is lengthy and often requires the patient to stay in the hospital for extended periods, undergoing complex and invasive evaluations. For example, intracranial recordings involve implanting electrodes inside the patient's brain, which can be both physically and emotionally taxing.

Despite these efforts, the mapping of the epileptogenic zones is often incomplete or inaccurate and the seizure freedom after a surgical procedure is around 65% (West, et al., 2019; Ayalon, et al., 2024). The perfect detection technology doesn't exist, and the medical teams need to rely on multimodal approaches. In addition, this approach requires excellent coordination between neuroradiologists, neurophysiologists, surgeons and all technicians involved. Also, most of those technologies are heavily dependent on users expertise, technical parameters and post processing techniques (Guerrini & Barba, 2021).

The success rate of epilepsy surgeries for FCD remains relatively low with a seizure free outcome for around 40% of the patients (Yao, et al., 2024). This is because the malformed brain tissues responsible for the seizures are often invisible to the naked eye and difficult to detect, even with

the most advanced imaging technologies. While preoperative brain mapping provides the surgeons with a general idea of the location of the epileptogenic zones, it is rarely precise. During the surgery, neurosurgeons face a significant challenge: they must carefully remove as much of the malformed tissue as possible without damaging healthy brain tissue. This task requires extreme precision because harming healthy tissue can lead to severe complications, such as loss of motor function, speech difficulties, or other neurological deficits. Unfortunately, the limitations of current techniques mean that some patients may require multiple surgeries, sometimes undergoing as many as four or more operations in their lifetime (Askoro, et al., 2024).

There is a critical need for the development of a reliable real-time intraoperative technique to detect the exact borders of FCD during surgery. Such a technique would allow surgeons to identify and remove the malformed tissues more effectively, improving the chances of success and reducing the need for multiple surgeries. Addressing this gap in medical technology could have a significant impact on the quality of life for patients with FCD and their families.

It is also important to note that FCD is the leading cause of refractory epilepsy in children (Najm, et al., 2022). This means that many young patients face the prospect of living with uncontrolled seizures and the associated risks, including developmental delays, learning difficulties, and a reduced quality of life.

2.2 Light matter interaction

2.2.1 Laser light and biological matter interaction

When light interacts with matter, several effects can take place depending on the energy of the incoming photons and the properties of the tissues and molecules being targeted. First, a part of the light is reflected, and the rest is transmitted to the tissue. The tissue surface layer has a different refractive index than air, silicon or glass, hence, considering a normal incidence angle, the reflectance R can be defined by the Fresnel equation that follows:

$$R = \left|\frac{n_1 - n_2}{n_1 + n_2}\right|^2$$

Where n_1 and n_2 the refractive index of the incident light and the tissue respectively.

The transmitted light through the tissue can be modelized as light transport through a turbid medium. In the near infrared (NIR) region, the diffusion approximation gives an accurate enough description of light transport in tissue:

$$\frac{1}{\nu}\frac{\partial \phi(\boldsymbol{r},t)}{\partial t} = \nabla \cdot D\nabla\phi(\boldsymbol{r},t) - \mu_a\phi(\boldsymbol{r},t) + S(\boldsymbol{r},t)$$

$$D = \frac{1}{3}(\mu_a + \mu_{s'})\ ;\ \mu_{s'} = \mu_s(1-g)\ ;\ \phi(\boldsymbol{r},t) = \int_0^{4\pi} L\,(\boldsymbol{r},\Omega,t)d\Omega$$

With ϕ the fluence rate in $W.m^{-2}$, L the radiance in $W.m^{-2}.sr^{-1}$, S the isotropic light source in joules, D the diffusion constant, μ_a the probability of absorption per unit of distance in m^{-1}, μ_s the probability of scattering per unit of distance in m^{-1}, g the anisotropy factor and ν the speed of light in the medium in $m.s^{-1}$ (Sandell, 2011). The anisotropy factor is defined as the average of the cosine angle of scattering angle. This factor is bounded between [-1, 1] which respectively correspond to maximum backscattering and maximum forward scattering. In biological tissues it is generally between 0.7~0.9 (Fukutomi, Ishii, & Awazu, 2016). The transport of light into tissues is then defined by μ_a and $\mu_{s'}$, absorbance and scattering, where $\mu_{s'}$ is more important than μ_a (Shapey, et al., 2022).

Table 1 Absorption and scattering optical properties of human grey matter. Data extracted from (Johansson, 2010)

Biological tissue	Wavelength [nm]	Absorption coefficient μ_a [cm^{-1}]	Reduced scattering coefficient $\mu_{s'}$ [cm^{-1}]
Grey Matter	480	3.7	12.1
	560	2.6	10.7
	580	1.9	9.9
	640	0.5	8.2
	780	0.2	7.8
	900	0.2	6.6

Absorbance occurs when the energy of the photon matches the difference in energy between the fundamental state and an electronic state of a molecule. In biological tissues, the main chromophores, molecules with high absorbance, are hemoglobin, water and melanin.

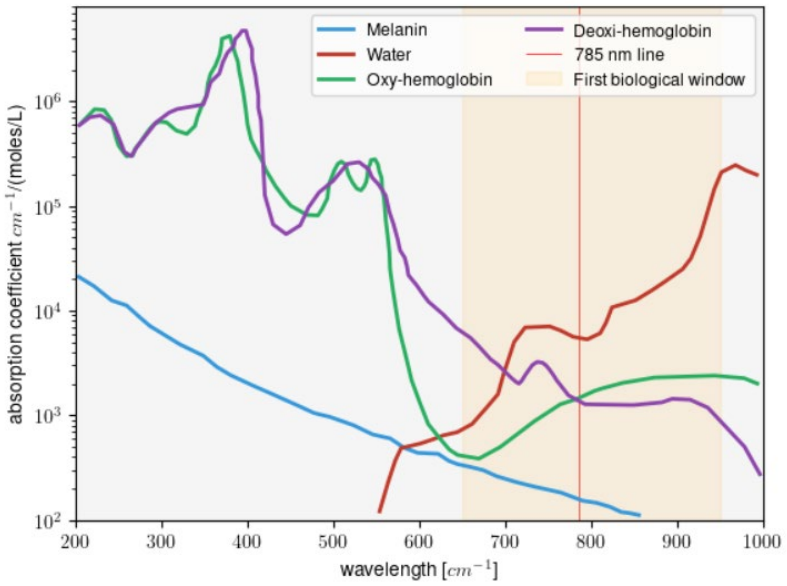

Figure 1: Absorption coefficient of principal biological human chromophores, data extracted from (Sandell, 2011). The 785 nm line corresponds to one of the main laser wavelength used in Raman spectroscopy.

The first optical therapeutic window corresponds to the [650, 950] nm region of the NIR spectrum where the absorption of the biological tissues is low enough to allow good light penetration and therefore facilitate imaging (Moreno, 2020). The non radiative deexcitations of the absorbed light produced heat, which can be sufficient to destroy cells and molecules. This effect can be used for therapeutic approaches (de Bie, et al., 2024) but can also be a source of hazard (Sowers, et al., 2022).

Scattering occurs when the energy of the incoming photon doesn't match the difference in energy between the fundamental state and an electronic state of a molecule. However, the light can still interact with the molecule, momentarily exciting it into a "virtual" electronic state. The molecule then almost instantaneously releases this energy in the form of radiation, a process referred to as scattering. The phenomenon can be modelized by Mie theory defining scattering particles as spherical objects. The parameter α, a dimensionless geometric parameter, is defined as follow:

$$\alpha = \pi D_p / \lambda$$

Where πD_p is the circumference of the particle and λ the wavelength of the incident photon. In the case of $\alpha \ll 1$, Rayleigh scattering is the main observable effect. For $\alpha \approx 1$or $\alpha \gg 1$, the main observable effects are respectively Mie and geometric scattering (Teich & Saleh, 2019). Rayleigh scattering is responsible for the color of the sky and Mie scattering for the color of the clouds. Both phenomena are elastic scattering effects, as the energy of the emitted photon is the same as the incident one. Another important metric about scattering, is that its intensity is inversely proportional to the wavelength of the incident light (Teich & Saleh, 2019) :

$$I = 1/\lambda^4$$

In parallel to those events, the energy of the emitted photon can differ from the incident one, it's inelastic scattering. If the emitted photon has less energy than the incident photon, the phenomenon is called Raman Stokes scattering. On the contrary, if the emitted photon has more energy than the incident photon, it is referred to as Raman anti-Stokes scattering.

Autofluorescence is another effect that takes place when laser light interacts with biological tissues. Molecules can absorb light, then have a partial non radiative deexcitation that leads to the emission of photons of different energy than the incident one (Teich & Saleh, 2019). Fluorescent molecules are characterized by excitation and emission spectra. The excitation wavelength influences the intensity of the emitted light, but the overall shape of the emission spectrum is molecule dependent.

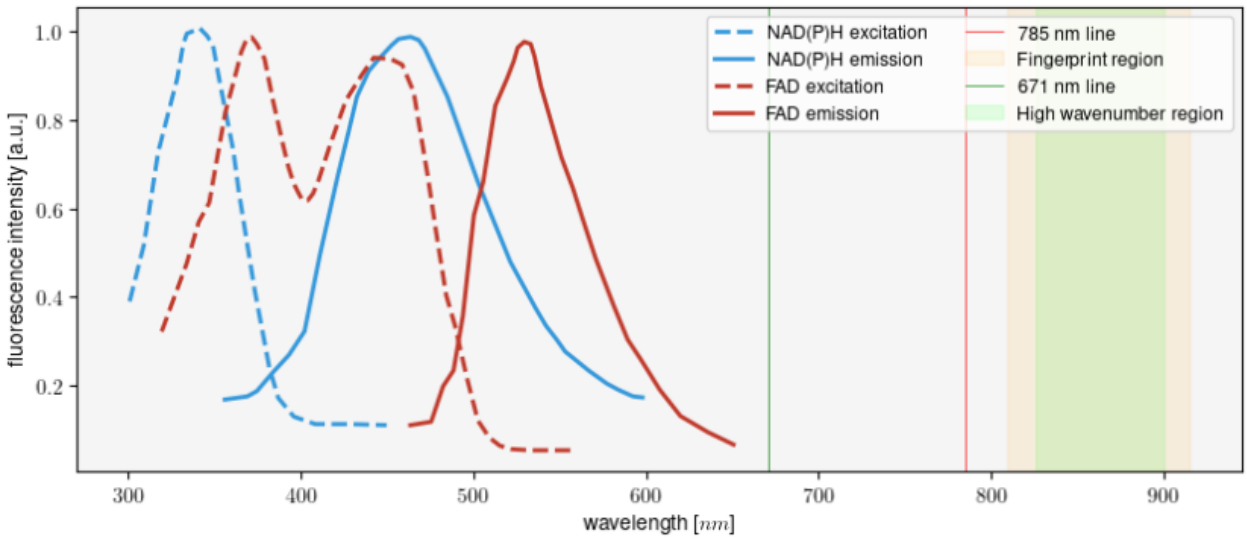

Figure 2 : Autofluorescence of two endogenic fluorophores data extract from (Lukina, 2016). The 785 nm and 671 nm lines correspond to the main laser wavelengths used in Raman spectroscopy. The fingerprint and high wavenumber region are here represented in their nanometer

range in respect to the excitation wavelengths of the lasers. The fingerprint region by the 785 nm laser and the high wavenumber region by the 671 nm laser.

The main endogenic fluorophores are nicotinamide adenine dinucleotide (NAD(P)H) and flavin adenine dinucleotide (FAD). Other flavins, collagen, elastin, tryptophan, lipofuscin and melanin are also endogenic fluorophores (Lukina Maria, 2021).

2.2.2 Raman spectroscopy

Raman spectroscopy is the study of matter at a molecular level using the eponym scattering effect. Within the NIR spectral range, two key regions are typically analyzed in biological applications: the high wavenumber region and the fingerprint region. Each of these spectral domains contains distinct molecular information and presents different advantages and challenges in clinical and research settings. The high wavenumber region extends from approximately 2800 to 3800 cm^{-1} and is characterized by vibrational information related to molecular bonds such as H_2O, CO, OH, and CH. This region has potential applications in specific biomedical contexts; however, its clinical utility is often limited due to its strong sensitivity to water content in tissues (Yang, 2022). Currently, Raman spectroscopy measurements in the high wavenumber region are typically performed using excitation sources at 671 nm in combination with charge-coupled device (CCD) detectors. Despite the advantages of this approach, a major challenge remains: the intensity of autofluorescence remains very strong at this excitation wavelength, significantly reducing the signal-to-noise ratio and affecting spectral quality (Aaboubout, et al., 2023). However, recent advancements in optical detection technologies, such as the development of indium gallium arsenide (InGaAs) detectors, when combined with a 1064 nm laser excitation source, present a promising avenue for overcoming these technological limitations. (Teich & Saleh, 2019). Although, the integration of this cutting-edge technology introduces numerous challenges that have already been addressed in existing, widely used systems. Overcoming these challenges requires catching up with years of prior research and development, which demands significant time and resources. Additionally, the lack of dedicated funding for NIR2 technologies further complicates its widespread implementation and slows down progress in the field. From the year 1990 to mid-February 2025, a PubMed search for the keyword "near infrared I" returns 82,826 entries, whereas "near infrared II" yields only 5,802 results. This marked contrast highlights the significant gap in research between the two regions. It further emphasizes the challenge of catching up with decades

of established knowledge while developing NIR-II technologies, which have yet to receive comparable levels of funding and scientific attention.

In contrast to the high wavenumber region, the fingerprint region spans from 400 to 2000 cm^{-1} and is commonly interrogated using a 785 nm laser. This spectral region is highly informative because it contains the characteristic vibrational signatures of numerous biologically relevant molecules, including proteins, lipids, and nucleic acids such as DNA and RNA (David, et al., 2023; Ember, et al., 2024; Huang, et al., 2012)**.** The fingerprint region is particularly advantageous for Raman spectroscopy in biological tissues, as it is largely insensitive to water content, making it highly suitable for *in vivo* and *in situ* applications where hydration levels can vary (Teich & Saleh, 2019). Although autofluorescence can still be present in the fingerprint region, its impact is less pronounced when compared to the high wavenumber region due to the use of a higher excitation wavelength.

Table 2 Bio markers detected in the fingerprint region taken from (David, et al., 2023; Ember, et al., 2024; Huang, et al., 2012)

Peak center (cm^{-1})	**Main vibrational modes**	**Tentative biomolecular assignment**
640	Tyrosine: Ring breathing	Proteins
785	Cytosine; uracil, thymine, cytosine: ring breathing (CU, CT, CC)	DNA/RNA
865	Ribose; C-C stretching, ring breathing, C=O stretching	DNA/RNA
937-942	Collagen; C-C stretching	Proteins
1002	Phenylalanine; symmetric aromatic ring breathing	Proteins
1004	Phenylalanine; C-C stretch	Proteins
1031	Phenylalanine; C-H deformation	Proteins
1081	Skeletal of acyl backbone; C-C stretching	Lipids
1129	Acyl backbone; C-C stretching, C-N stretching,	Lipids
1176	Cytosine, thymine, guanine; C-H bending	DNA/RNA
1208	DNA/RNA bases; ring breathing, C-N stretching Phenylalanine, tyrosine	DNA/RNA, proteins
1246, 1266	Amide III	Proteins
1299-1301	CH_2 deformation & plane twisting	Lipids
1301-1304	C-H vibration	Lipids
1336-1340	Tryptophan; CH_2 / CH_3 wagging & twisting	Proteins
1441-1453	CH_2 / CH_3 deformation; C-H bending	Lipids, proteins
1600	Phenylalanine; C=C	Proteins
1656	Amide I; C-O stretching	Lipid, protein

CHAPTER 3 RAMAN ACQUISITION SYSTEM

3.1 Spectrometer and probe

The system currently being used for this clinical study has undergone several improvements compared to the previous technologies that were used by our laboratory in earlier projects. In the past, our group used Class I systems. These systems were used in a variety of settings, including both *in vivo* (intraoperative) and *ex vivo* clinical studies (Desroches, et al., 2019; Desroches, et al., 2015; Ember, et al., 2024). The new class of systems, which are now classified as Class II, have received significant changes to their optical design.

The main purpose of these modifications was to optimize the efficiency of light collection in order to improve the overall performance of the system. They ensure that the Class II system could achieve the same levels of signal-to-noise ratio (SNR) as the previous Class I systems while also reducing the overall imaging time. These enhancements not only improve the system's performance but also make it more efficient and suitable for use in real-time clinical applications, which is critical for the success of the study.

3.1.1 Class I Raman handheld single point probe system

The Raman spectroscopy system that belongs to Class I have been described in detail in previous works made by our group (David, et al., 2023; DePaoli, et al., 2020). Briefly, these systems consist of several key components. A hand-held probe manufactured by EmVision LLC, based in Florida, USA. This probe is coupled with a spectrally stabilized laser (Innovative Photonic Solutions, New Jersey, USA), which emits light in the NIR spectrum at a wavelength of 785 nm. Additionally, the system includes a high-speed and high-resolution charge-coupled device (CCD) camera (ANDOR Technology, located in Belfast, UK). The data acquisition is managed through specialized software, which allows for each data collection session to be conducted at a pre-determined laser power level at the tip of the probe (I) and for a specific accumulation time (T). This process can be repeated a set number of times (N) to optimize the SNR for each acquisition.

The hand-held probe itself is made up of nine collection fibers, each with a 300-micron core diameter. These fibers are arranged around a donut-shaped long-pass filter. This filter plays a critical role by blocking the laser light while allowing Raman light from the sample to pass through

to the collection fibers. The collection fibers encircle a stainless-steel tube, which houses the laser delivery fiber assembly. The laser delivery fiber has a 200-micron core and features a small band-pass filter positioned in front of it to eliminate any Raman signals generated within the fiber. The front optical assembly consists of a two-piece converging lens system. The back portion is a plano-convex lens made of sapphire, with a 2 mm diameter curvature, chosen for its high refractive index, which sharply bends the incoming light. The front portion is a flat, 1 mm thick lens made of plano magnesium fluoride. This lens configuration was designed to ensure precise overlap between the focus of the excitation light source and the region from which the Raman light is collected at the sample surface. Importantly, this overlap occurs without any interference caused by the sapphire lens, which ensures accurate and efficient measurements. The connector of the Raman probe to the spectrometer contains the collection fibers only. These fibers are securely housed within a specially designed spring-loaded snap-in connector in a vertical alignment that fit the spectrometer entrance slit. This connector not only provides a stable and reliable structure for holding the fibers in place but also facilitates assembly during the setup process. The spring-loaded mechanism allows for a secure fit when connecting the probe to the spectrometer, minimizing the risk of misalignment or damage to the fibers. This design feature contributes to the robustness of the system, making it easier to handle and assemble while maintaining the high level of precision required for Raman spectroscopy measurements.

The Class I spectrometer is designed with a specific configuration to ensure optimal performance during Raman spectroscopy measurements. It features a 100-micron slit designed to fit the collection fibers arrangement from the probe connector, but also minimizes the amount of ambient light entering the spectrometer. This slit is precisely 3.25 mm tall, a dimension that has been optimized to balance light throughput and spectral resolution. The spectrometer also features a high pass filter that cuts the laser line that could have entered the collection fibers. The rest of the optical system is made of lens focusing the light on the grating and then lens focusing the diffracted light on the CCD.

3.1.2 Class II Raman handheld point probe system

The Class II probe introduces several innovative modifications aimed at improving its overall performance and minimizing sources of interference. One of the key changes is the incorporation of a hole within the converging lens. It allows the laser excitation light to pass directly through the

lens, which effectively reduces laser reflections from the lens surfaces. By removing these reflections, the amount of scattered laser light within the probe is significantly reduced. Additionally, the new probe design includes a donut-shaped lens filter, which plays an important role in blocking any backscattered laser light originating from the tip of the probe or the sample itself. Those improvements minimize the interference caused by scattered laser light interacting with the probe's internal materials, enhancing the overall signal quality. Another improvement is the use of a stepped window. This feature reduces the window diameter, which helps to limit the collection of unwanted light from areas outside the designated sample spot. The stepped window is also filled with window block material, which is specifically designed to maximize stray light rejection. This ensures that only the relevant signal from the sample spot is collected, further improving the performance of the probe. Finally, the new probe design incorporates an increased number of fibers, from nine to twenty-one 300-micron core fibers, which has led to a slight increase in the probe's diameter. While the Class I probe has a diameter of 2.1 mm, the new probe has a diameter of 2.4 mm. To accommodate this change, several modifications to the overall probe have been made. At the tip of the probe, the collecting fibers are placed in a double ring formation around the laser fiber. The connector part of the probe also had to be modified. It is now bigger and sturdier. The collecting fibers couldn't be arranged in a unique vertical configuration. Instead, they are in three symmetric vertical configurations of seven fibers. The spring-loaded mechanism have been replaced by a simple snap-in one.

The Class II spectrometer is designed with several enhancements compared to the Class I spectrometer to improve its performance and accommodate the new probe's increased capabilities. One of the key features of the Class II spectrometer is its connector, which includes a 250-micron slit with a height of 7.6 mm. This larger slit size is a significant design change that enables the spectrometer to handle a greater amount of incoming light.

To support the increased number of input fibers used in the Class II system, larger lenses were custom-designed and manufactured specifically for this spectrometer. These lenses play a critical role in optimizing light collection and transmission. They are designed to reduce the actual 250-micron slit width of the Class II spectrometer to approximately the same slit image size as that of the Class I spectrometer when projected onto the CCD detector. This optical adjustment ensures that the system maintains a high level of efficiency and compatibility despite the increased input capacity. The larger slit width of 250 microns in the Class II spectrometer allows more than double

the amount of light to enter the spectrometer compared to the Class I design. Importantly, this increase in light input does not compromise the spectral resolution, which remains like that of the Class I spectrometer. To accommodate the larger lenses and the more complex optical components required for this enhanced design, the Class II spectrometer features a larger enclosure footprint.

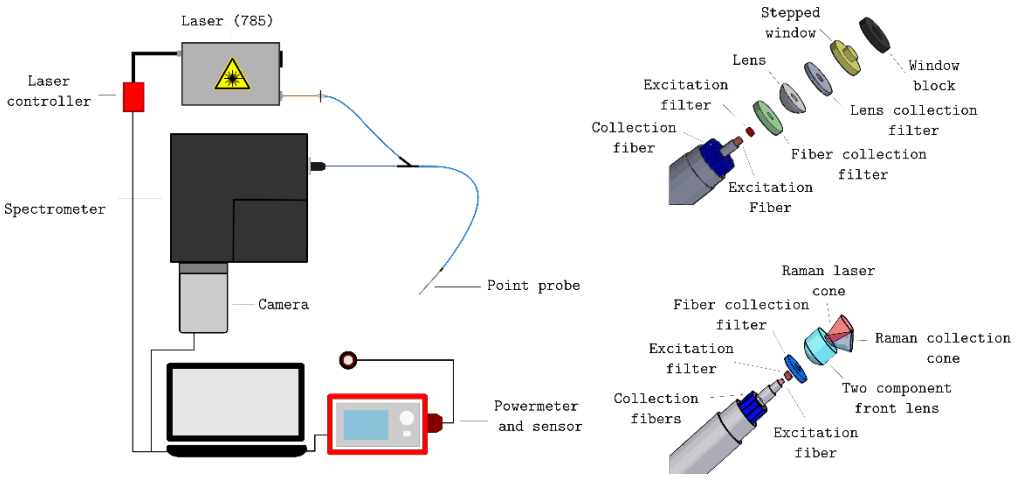

Figure 3 : Composition of a handheld single point system and architectures of class 1 and 2 probes. In its simplest form, a Raman handheld single point probe system is composed of a camera CCD, a spectrometer, a laser source and a fiber optic probe. The tip of the probe is a combination of an excitation fiber, collection fibers, filters and lenses.

3.2 Experimental protocol of the characterization of the performances of the Class II system

Class 1 and 2 systems were compared using a one-centimeter-deep store-bought olive oil sample. It is an organic material with a strong Raman signature and a high fluorescence background. A black coated aluminum substrate was used as a container. Its low background signature makes it ideal compared to other substrates such as glass. Both probes were positioned in contact with the surface of the olive oil sample, and measurements were performed using a fixed laser power set at I=50 mW and number of repeated measurements per acquisition at N=25. For each acquisition, different exposure times were tested, starting at a T low value and increasing in increments of 10 milliseconds until the signal reached saturation.

Once the measurements were collected, standard data processing steps were applied to each individual data set. These processing steps included calibration of the x-axis (wavelength or Raman shift) and y-axis (signal intensity) to correct for systematic errors, as well as the removal of cosmic ray artifacts that could interfere with the data. After these preprocessing steps, the Raman spectra

resulting from the measurements are averaged across the N repeated measurements for each exposure time. Additionally, the standard deviation of the signal is calculated for each spectral bin to assess the variability of the measurements. The final processed spectra spanned the Raman shift range from 400 to 2000 cm^{-1} and had a spectral resolution of approximately 5 cm^{-1}.

In order to compare the two probes, two main characteristics were calculated. The first metric is the evolution of the quality factor (QF) along the integration time. The QF is defined as the average signed square intensity (Sheehy, et al., 2023) :

$$QF = \frac{1}{M}\sum_{i=1}^{M} sgn(r_i^\star) \cdot r_i^{\star 2}$$

Where $r^\star$ is a standard normal variate (SNV) normalized processed Raman spectra, $sgn(x)$ the sign function that gives -1 or 1 depending on the sign of x and M the number of bins across the x-axis. SNV normalization consists on setting the mean and standard deviation of the spectrum to respectively zero and one.

The second metric is the maximum maximum intensity of the non-normalized Raman spectra across the integration time.

3.3 Results and validation

The Raman spectra obtained from both the Class 1 and Class 2 devices were plotted for exposure times of 50 milliseconds, 100 milliseconds, and 150 milliseconds.

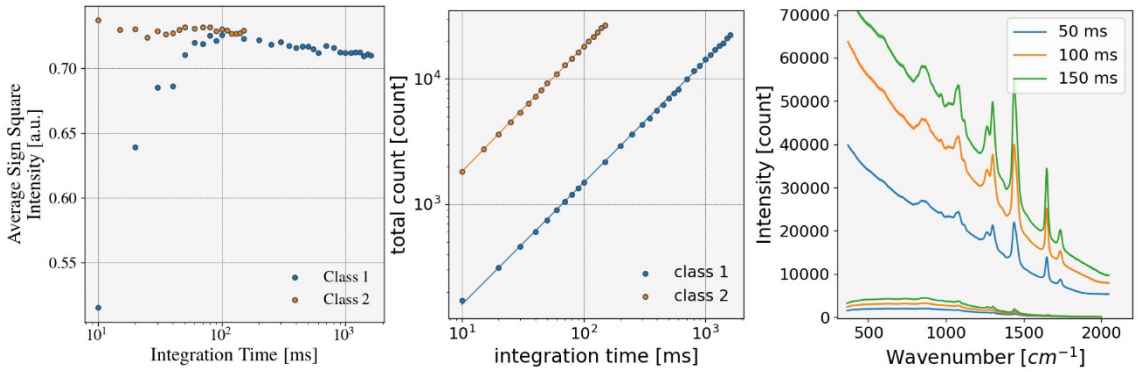

Figure 4 : Metrics comparison of class I and II probes. From left to right, ASSI on integration time; max Raman count on integration time; Class I and II system corrected raw spectra for 50, 100 and 150 ms.

From these plots, it was observed that the Class 2 probe consistently acquired a signal that was more than one order of magnitude larger than the signal obtained with the Class 1 probe, even when the same laser power and exposure times were used. To further illustrate this difference, the overall photon count corresponding to the Raman signal detected by each probe was plotted as a function of exposure time. In this plot, the y-axis (photon count) was presented on a logarithmic scale for better visualization of the differences (Figure 4). The photon count values plotted corresponded to the Raman signal after the fluorescence background was removed using a specialized algorithm called the BubbleFill algorithm which have been extensively described in this publication (Sheehy, et al., 2023). This analysis confirmed that the Raman signal due to inelastic scattering, after fluorescence background removal, was more than ten times higher for the Class 2 probe compared to the signal obtained with the Class 1 probe.

Representative spectra were selected to further highlight the differences in performance between the two probes. One spectrum was acquired with the Class 1 probe using an exposure time of 1000 milliseconds, and another spectrum was obtained with the Class 2 probe using a significantly shorter exposure time of 150 milliseconds. For both spectra, the SNR was calculated for two prominent lipid bands: one centered at 824 cm^{-1} and the other centered at 1440 cm^{-1}. For the lipid band centered at 824 cm^{-1}, the SNR was found to be 110 for the Class 1 probe and 118 for the Class 2 probe. Similarly, for the lipid band centered at 1440 cm^{-1}, the SNR was measured as 540 for the Class 1 probe and 584 for the Class 2 probe.

These results, derived from the two representative spectra, demonstrate that the signal quality (as indicated by the SNR) was equivalent between the two probes. However, the Class 2 probe was able to achieve this level of signal quality with exposure times that were more than ten times shorter than those required by the Class 1 probe. This significant reduction in integration time highlights the enhanced efficiency of the Class 2 probe, making it a more effective tool for Raman spectroscopy applications.

CHAPTER 4 CLINICAL STUDY

4.1 Integration of the system into the clinical workflow

4.1.1 Validation of the usage of the system in the hospitals

The system in use has been deployed in three different hospitals, *Hopital Maisonneuve-Rosemont* for a previous study, *Centre hospitalier universitaire Sainte-Justine* and the *Centre universitaire de santé McGll* for the current study. For the three hospitals, the first step was to verify the electrical compliance of the whole system. A medical grade electrical transformer (AMGIS MEDBOX) which respects the C-UL-US certification has been used. In each situation, the biomedical engineering department gave the approbation to use the system in the operating room.

The second step was to validate the sterilization process with the MDRD. The probe needs to be cleaned of all residual blood, tissues and stains. This process is made by hand with neutral cleaning products and soft cloths. The technicians must be careful to only immerge in water the part of the probe where all the fibers and optics are compartmented in a single cable and the tip of the probe. As some of the elements are heat sensitive, the probe can't be sterilized by autoclave and low temperature sterilization processes are needed. The manufacturer identified the STERRA 100S, STERRAD NX, STERRAD 100NX and the STERIS AMSCO V-PRO® MAX as compatible with the needed sterilization process. Each of the medical centers where the probe was used had at least one of those.

A sterilization tray commissioned from *Trudell Solution Santé* has been provided for each study center. The elements were chosen with the help of a surgeon and the manager of the *Hopital Maisonneuve-Rosemont's* MDRD head technician.

The last step was to verify the different rules to follow in each OR and to decide who gets the responsibility of the probe. For the *Hopital Maisonneuve-Rosemont's* and the *Centre universitaire de santé McGll*, making sure the probe was sterilized before the case and bringing it back to the MDRD is the responsibility of system operator. For the *Centre hospitalier universitaire Sainte-Justine*, the probe is taken care of by the medical team. For all study centers, the rules inside the OR are similar; never touch the blue drapes, try to always face the blue drapes, keep a 20-centimeter distance between you and the blue drapes. They correspond to the sterile zone of the OR. At last, keep your hands close to your torso and head nurse have full authority inside the OR.

4.1.2 Operating room protocol

Before entering the operating block, scrubs or a disposable protective suit must be worn, along with a surgical mask, shoe covers, and a surgical cap or mobcap. The acquisition system ; including the computer, cart, laser, power meter, camera, spectrometer, electrical transformer, should be sanitized with cleaning wipes. These precautions ensure a minimal standard of cleanliness in the operating room, reducing the presence of dust, dirt, and bacteria around patients.

Since an operating room differs from an optical laboratory, the acquisition protocol must be adapted to prioritize the safety of patients and all users around them. To maintain the sterility of the probe, laser calibration cannot be conducted prior to *in situ* use and must instead be performed following all the samples acquisitions. This is managed by using the calibration from the previous case and correcting it afterward with a new one. Acquisition parameters are set to limit laser exposure to no more than 85% of the maximum permissible level, by that, any uncertainties in laser power are accounted for.

Before connecting the probe and starting the measurements, the camera sensors are first cooled to -70°C. Preliminary acquisitions are performed without turning on the laser to ensure that the system is operating correctly.

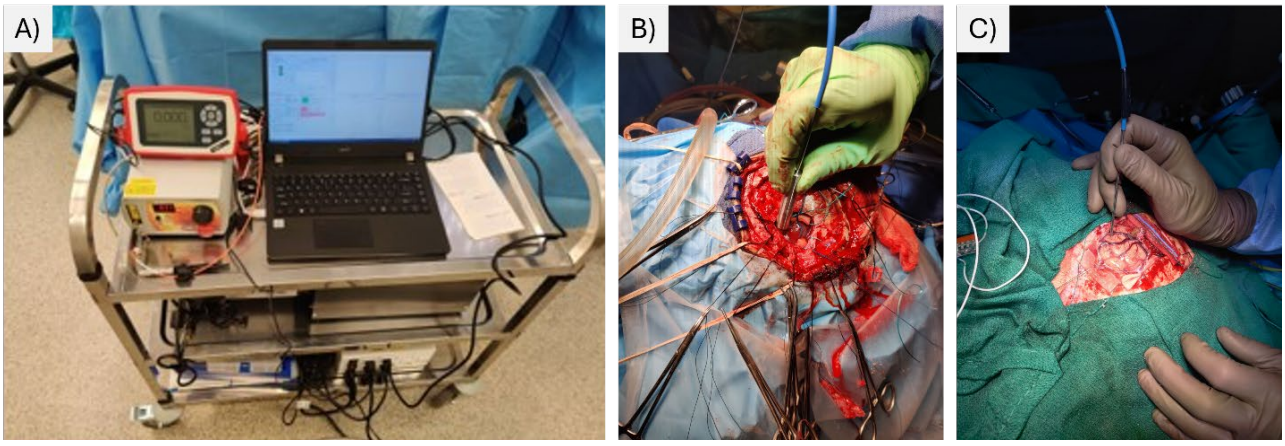

Figure 5: Clinical research Raman handheld system and point probe in contact with brain. A) The actual medical grade Raman system used for the study placed near blue drapes ready for taking acquisitions. B) Point probe with its experimental stainless light shield used at CUSM. C) Point probe used at CHUSJ.

Over the course of different clinical cases, refinements to the acquisition protocol have been developed, with the goal of minimizing disruption to the surgical procedure while maximizing spectral quality and ensuring safety. During surgery, the surgeon selects an area for resection that is suitable and relevant for study. The probe is placed in contact with the selected area, and the sample name is stated aloud for the nurse and spectroscopy system user. It is the name used in the pathology report. To minimize ambient light, neon lights are turned off, scialytic lights are dimmed or switched off, neuronavigation equipment is repositioned, and surgeon headlights are switch off. Before beginning the acquisition, the surgeon gives verbal confirmation that they are ready, and system user provides updates when the acquisition takes place, as well as when the laser is deactivated. Lights are then switch back on, the surgeon completes the resection, and the sample is handed to the nursing staff. This process may be repeated up to ten times during a single surgery.

The acquisition volume is around 500 μm^3 while the resected samples sizes vary between 1mm to 2cm. The surgeon selects tissues depending on if they are in the EZ or not and in the same area of the brain. Those are considered homogenous.

Post-surgery, tissue samples are sent by the surgical team to the pathology department. Upon receiving the pathology report several days later, tissue labels are assigned to the acquired spectra. A histology analysis is performed on each resected sample using hematoxylin and eosin staining technique. From this examination, pathologists redact a report where each specimen get a unique label assigned to it.

4.2 Assessment after 2 years

4.2.1 Clinical cohort

This study examined the use of the Class II Raman spectroscopy system during intraoperative procedures involving 23 pediatric patients who underwent brain surgery at the CUSM and CHUSJ. The patient cohort consisted of children experiencing epileptic seizures, with the majority having a strong indication of FCD.

Table 3 Summary of the cohorts from the CUSM and CHUSJ

	CUSM	**CHUSJ**
Number of patients	19	4

Focal cortical dysplasia	16	4
Glioma	1	-
Glioblastoma	1	-
Embryonal tumor	1	-

4.2.2 Raman spectral acquisition

On average, six spectra were acquired during each clinical case, with the number of spectra ranging from a minimum of two to a maximum of sixteen. The standard deviation observed across the cases was 3.6. This variability can be attributed to differences in the clinical context and the accessibility of the target tissues during each procedure.

Table 4 Numbers of samples for each pathological classification

Diagnosis	**CUSM**	**CHUSJ**
FCD	30	-
Non definite feature of FCD	5	-
Normal brain	39	31
Glioma	3	-
Glioblastoma	2	-
Embryonal tumor	5	-

Non attributed	54	5
Number of acquisitions	133	36

It is important to note that the rarity of the malformation, combined with the inherent challenges involved in accurately identifying and assessing its presence during surgery, significantly influenced the data collection process. As a result, the number of measurements obtained from tumoral brain tissue compared to non-tumoral brain tissue was not as balanced as initially intended. This imbalance highlights the complexity of studying rare neurological conditions and the limitations faced when attempting to collect evenly distributed data in such a clinical setting.

This imbalance also contributes to the presence of non-attributed classifications, which refer to Raman measurements that were not linked to a specific pathological classification. In most instances, this occurred because the surgeon chose not to proceed with the resection after the acquisition. However, for three patients, among the nineteen, at the CUSM, it appears that no pathological report from their internal system corresponds to the acquisitions taken during the procedure.

Brain cancer samples from patients having seizures were acquired and compared with results from the previous adult brain study performed by the laboratory. However, those results are not reported in this thesis.

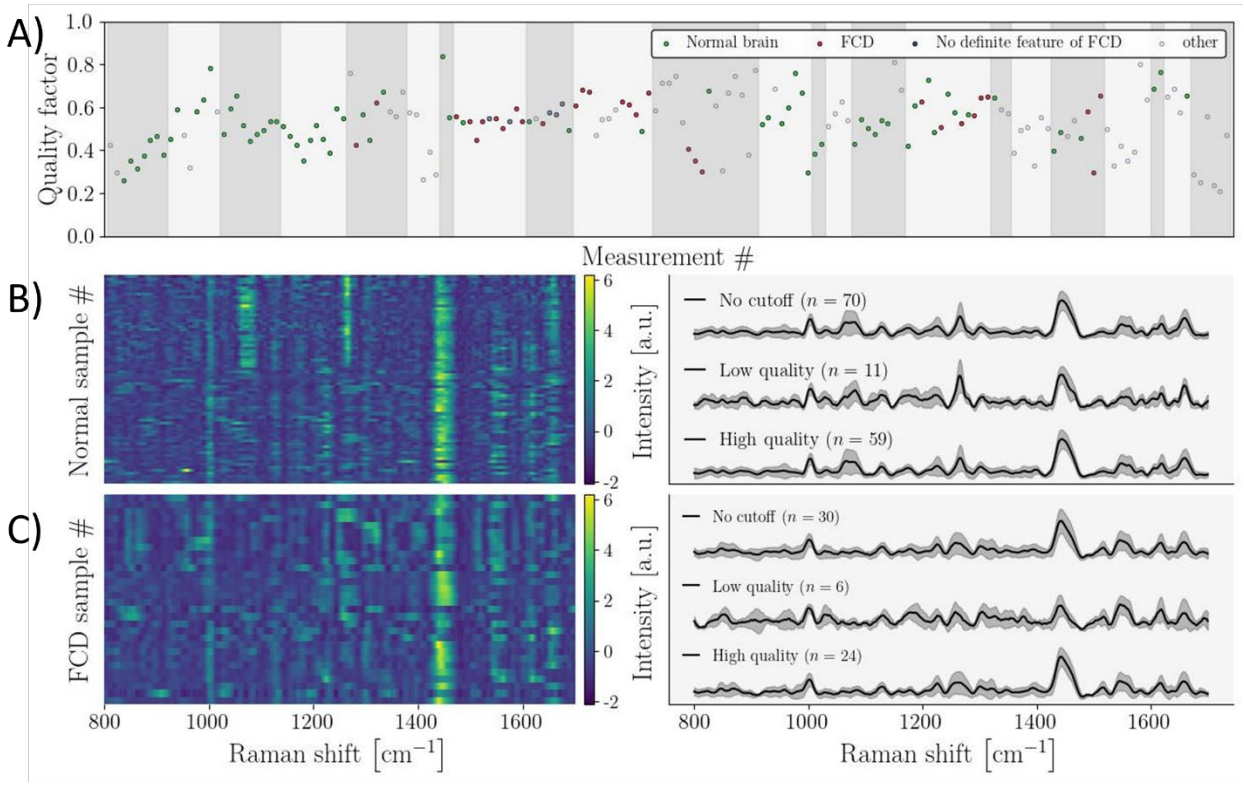

Figure 6 : Depiction of the spectral quality of the acquisitions taken during the clinical trial. A) Quality factor, B) Spectrogram of normal brain samples and the mean spectra of this category for no quality factor cutoff, low quality factor and high-quality factor. C) Spectrogram of FCD brain samples and the mean spectra of this category for no quality factor cutoff, low quality factor and high-quality factor.

Each acquisition has been made with a laser power of 50mW at the probe tip with a exposition time automatically selected to maximize 85% of the dynamic range of the camera. The number of successive spectra per acquisition is determined to respect the Maximal Permissive Exposure of the skin for an acquisition surface of 3.5 mm square using the following equation:

$$P(Nt)^{0.75} < 0.186$$

With P the laser power, N the number of spectra for the acquisition and t the integration time of each pulse.

The **Figure 5**.A depicts the QF for each acquisition across the dataset. Grey and white bars correspond to the different patients, with the first four ones from the CHUSJ. For this study, a QF above 0.4 is considered good, which corresponds to most of the dataset. The spectrograms, in the Figure 5.B and C, of the normal and FCD brains looks uniform except for the area around 1070

cm^{-1} and 1260 cm^{-1}. There is a visible anomaly in the CHUSJ dataset. However, for the purpose of this study it was deemed reasonable to ignore those regions. Some additional test should be done before integrating those spectra into a machine learning algorithm.

In addition to the spectrograms, the graphs on the left show mean spectra of FCD and normal brain acquisitions. The upper curve corresponds to the mean spectrum of all acquisitions without cutoff. The middle curve corresponds to the mean spectrum of acquisitions where the QF is lower than the 0.4 threshold, those are the lowest quality measurements of the dataset. The lower curve corresponds to the mean spectrum of acquisitions where the QF is superior to the 0.4 threshold, those are the highest quality measurements of the dataset. For the following statistical analysis of the dataset, only the high-quality spectra are used.

4.2.3 Statistical analysis of FCD/Normal dataset

A Mann-Whitney U test is applied to each bin of the dataset with the aim of identifying biological markers that could potentially differentiate FCD tissues from normal brain ones. This statistical method is employed to determine whether two independent samples come from the same population or not. In this context, the dependent variable corresponds to the intensity of each spectral bin, which is measured across the entire population, while the independent variables are the two distinct groups. The dataset satisfies the necessary assumptions for conducting a Mann-Whitney U test. Specifically, the dependent variable is continuous and ordinal. Furthermore, the intensity distribution of each bin is expected to follow a non-normal distribution, as the measurements are acquired at different times on separate brain samples. This variability, inherent in the data collection process, makes the assumption of normality unsuitable, which aligns with the purpose of using the Mann-Whitney U test. It is also assumed that the dataset size is sufficiently large to ensure the validity of the test and to provide reliable results. The null hypothesis of the test states that the two groups of the dataset come from the same population, implying no significant difference in their Raman spectra. To assess the significance of the differences between the groups, the p-values calculated across the entire Raman shift axis are plotted in Figure 6, providing a visual representation of the statistical comparison. The resulting p-values will be used to determine which

bins show statistically significant differences in intensity, indicating potential biological markers for distinguishing FCD tissues from normal brain ones.

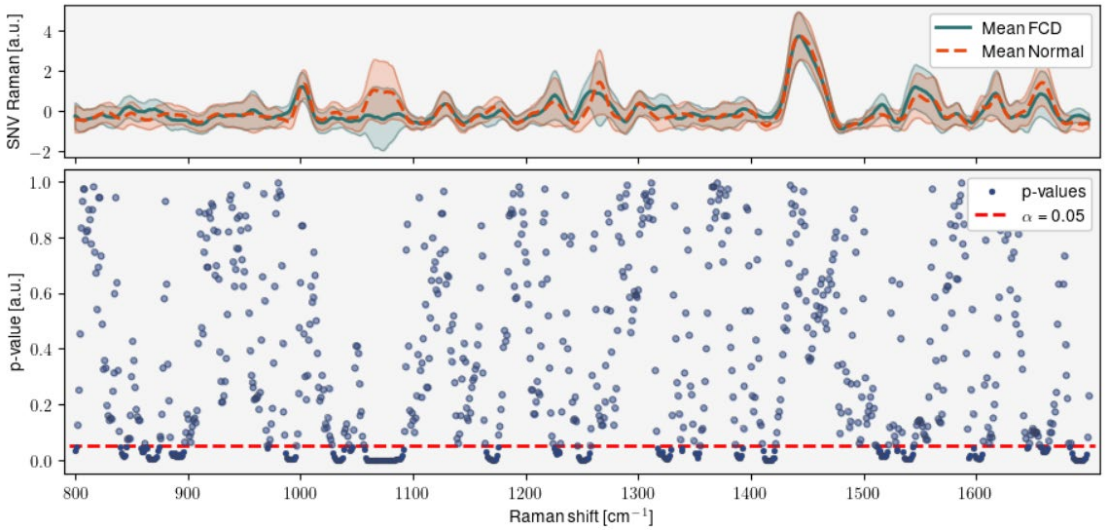

Figure 7 : P-values of a Mann-Whitney U test for each spectral bin across the [800-1800] cm^{-1} range. Top graph is the mean SNV normalized spectra of all FCD and normal samples with their standard deviation. In the bottom graph, the p-value lower than α are emphasized.

The threshold for rejecting the null hypothesis is set at a significance level $\alpha = 0.05$, meaning that if the p-value is lower than this threshold, the FCD dataset can be considered statistically different from the normal brain dataset with a confidence level of at least 95%. This threshold ensures that the observed differences in Raman spectra are not due to random chance but represent a true distinction between the two tissue types. Following this, the next step involves manually selecting spectral bins that exhibit low p-values, as these are likely to correspond to biological markers that distinguish FCD tissue from normal brain tissue. This selection process is critical as it helps to reduce the number of parameters being analyzed, focusing only on the ones that show significant differences. By concentrating on these key spectral features, we can avoid including noise or irrelevant data that could lead to incorrect classifications. Moreover, it will allow for a better understanding of which biomolecular marker families are more prominently associated with one category compared to the other. Additionally, it offers the opportunity to verify the consistency and coherence of the findings with other Raman spectroscopy studies on FCD.

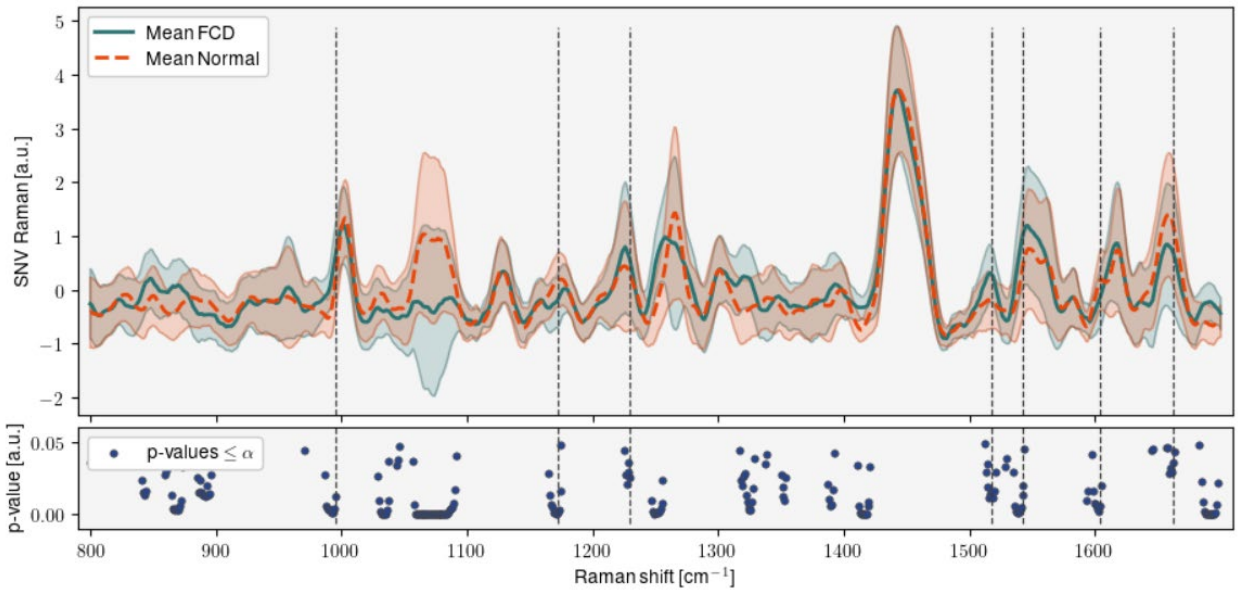

Figure 8 : Seven selected spectral bins that reject the null hypothesis with confidence superior to 95%. Peak center of selected bins, from left to right: phenylalanine (1002 cm^{-1}) ; C-H bending tyrosine, cytosine and guanine (1176 cm^{-1}) ; phenylalanine (1208-1220 cm^{-1}) ; cytosine (1520 cm^{-1}) ; adenine and guanine (1570 cm^{-1}) ; phenylalanine (1600 cm^{-1}) and amide I (1656 cm^{-1}). **(David, et al., 2023; Ember, et al., 2024; Huang, et al., 2012)**

The selected peaks are primarely associated with proteins and DNA/RNA biomarkers. The only exception is the amide-I peak at 1656 cm^{-1}, which is linked to lipids. All these peaks are recognized as Raman biomarkers and have p-values that fall below the threshold limit, indicating their statistical significance.

One observation is that the spectral bins with the lowest p-value are not located at the center of the biomarker's peaks. More than the intensity, the shape of the peaks themselves are a major factor in differentiating the two similar tissues. Peak fitting theory for Raman peaks found that they can be fitted by either a Gaussian function, a Lorentzian function or a mixed function called Voigtian (Yuan & Mayanovic, 2017). The Gaussian function is associated with solid samples and the Lorentzian one with liquid and gaseous samples (Tuschel, 2021). In addition, the natural Raman relaxation from the virtual state and the dephasing of molecules both have an impact on the width of the peaks and are also linked to the state of the tissues (Tuschel, 2021). The width and general shape of the different peaks can present more differences than their maximum peak intensity.

The following step involves examining the distribution of the selected spectral bins to further analyze their characteristics.

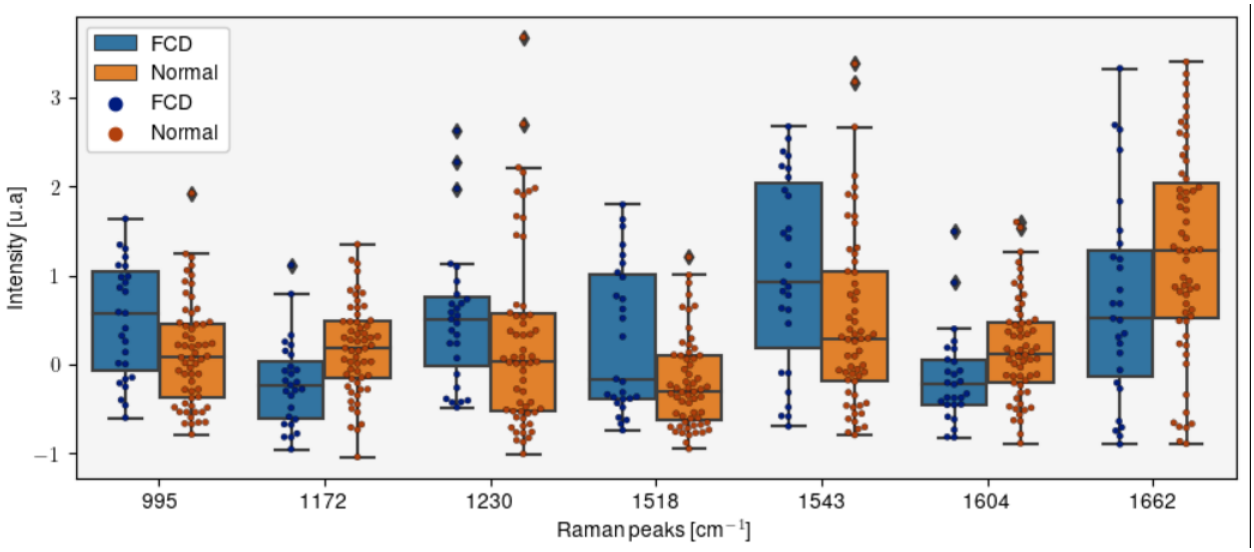

Figure 9 : Box plot of the intensity of the selected spectral bins for the power study on High QF spectra. The rectangles are the interquartile range divided in the lower hinge, the median and the upper hinge. Lower and upper whiskers correspond to the boundaries before data points are considered outliers. Points show the actual distribution of the data.

For the 995 cm^{-1} spectral bin, the median value for FCD tissue lies outside the interquartile range of the normal brain sample, indicating a potential distinction between the two groups. However, this pattern is not observed reciprocally. In contrast, for the 1172 cm^{-1} and 1604 cm^{-1} spectral bins, both the median values for FCD and normal tissues fall outside the interquartile range of the respective groups. This observation suggests a more pronounced difference between the two tissue types for these peaks. Moving to the 1518 cm^{-1} and 1543 cm^{-1} spectral bins, it is apparent that the FCD data is much more dispersed compared to the normal brain data. Similarly, for the 1662 cm^{-1} spectral bin, both distributions are highly dispersed, although the FCD data seems to exhibit greater variation. On the other hand, the 1172 cm^{-1} and 1604 cm^{-1} spectral bins shows the lowest dispersion across both groups, which may point to a more consistent spectral feature. Overall, the data shows greater dispersion than that observed in previous studies by our research group (David, et al., 2023; Ember, et al., 2024), particularly within the FCD group. This increased dispersion is likely due to the smaller sample size in this current study.

In addition to their dispersion, the actual shape of the data distributions can provide valuable insights into the spectral bins, offering further context for interpreting the differences observed

between FCD and normal brain tissues. Understanding these distribution patterns is crucial for deeper interpretation and is explored in greater detail in the Figure 9.

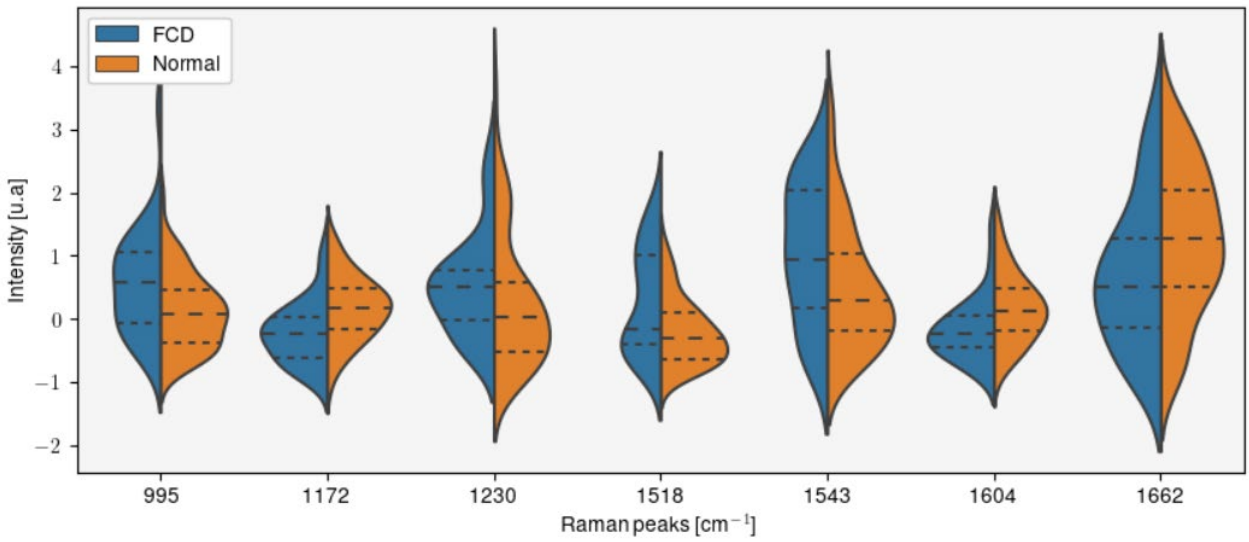

Figure 10 : Violin plot of the intensity of the selected spectral bins for the power study on High QF spectra. The dash lines correspond to the first quartile, the median and the third quartile. The violin shapes are kernel density approximation of the data distributions. It can be seen as a smooth version of the histogram from the same dataset.

With enough data samples, we would expect the distributions of the spectral bins to exhibit bell-shaped curves or right/left skewed shapes. The 1172 cm^{-1} and 1604 cm^{-1} spectral bins display relatively clean curves or slightly skewed shapes, indicating a more typical distribution pattern. On the other hand, both 1230 cm^{-1} and 1518 cm^{-1} follow a bimodal distribution. The remaining spectral bins show distributions that resemble a bell curve but with some characteristics of a bimodal or multimodal distribution. These variations suggest that the dataset lacks sufficient samples, particularly within the FCD group. However, despite this, the 1172 cm^{-1} and 1604 cm^{-1} stand out. They both exhibit medians outside of the interquartile range for both groups, show lower dispersion compared to other bins, and possess distribution shapes that are more in line with what is expected. These two spectral bins, therefore, appear to be the most reliable indicators of the differences between FCD and normal brain tissue.

One key conclusion of this analysis is that the dataset is missing a number of samples. To estimate how many samples the study would ideally need, an A-Priori t-test was conducted using the G*Power software (Bruin, 2011). The test was performed on the 1172 cm^{-1} and 1604 cm^{-1} spectral bins, if the normal-to-FCD sample ratio $^{\#normal}/_{\#FCD} = 2.45$ would remain constant as the

number of samples increases. Based on the test results, the software suggests that 350 and 850 samples would be needed for the 1172 cm^{-1} and 1604 cm^{-1} spectral bins, respectively, to achieve adequate statistical power. These findings highlight the need for a larger dataset to ensure more reliable statistical analyses and strengthen the validity of the observed spectral differences between FCD and normal brain tissue.

Despite the limited sample size, it is still possible to establish a preliminary benchmark for distinguishing FCD from normal brain tissue. By leveraging the 1172 cm^{-1} and 1604 cm^{-1} spectral bins, a classification framework can be developed, providing a valuable foundation for further refinement as more data becomes available. For each spectral bins, an intensity threshold can be defined to categorize true positives (TP), true negatives (TN), false positives (FP) and false negatives (FN). Measurements with intensities below the threshold are classified as FCD (positive), while those above the threshold are classified as normal brain tissue (negative). To evaluate the classification performance, a receiver operating characteristic (ROC) curve can be generated by systematically varying the threshold from the minimum to the maximum intensity values observed in both groups. The false positive rate (FPR) and true positive rate (TPR) are then calculated across this range to assess the model's ability to differentiate between the two tissue types.

$$1 - specificity = FPR = \frac{FP}{FP + TN} = 1 - \frac{TN}{FP + TN}$$

$$sensitivity = TPR = \frac{TP}{TP + FN}$$

The optimal classification threshold is determined by finding the intensity value, x, that maximizes the difference between the TPR and the FPR. This corresponds to the point where $TPR(x) - FPR(x)$ reaches its highest value within the intensity range, ensuring the best balance between sensitivity and specificity.

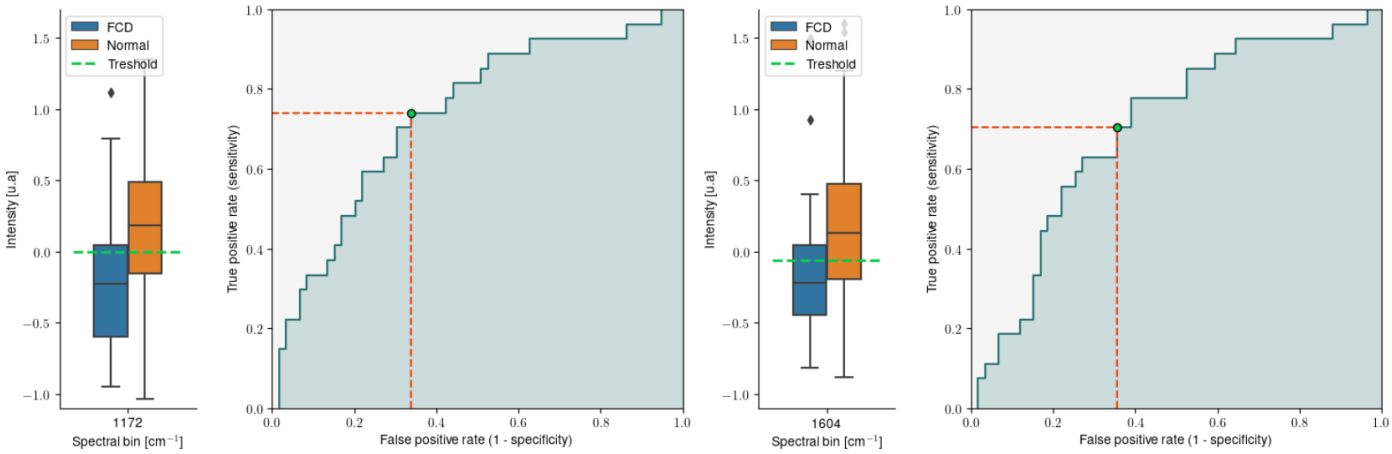

Figure 11 : ROC curve of the 1172 cm^{-1} and 1604 cm^{-1} spectral bins. The red line dividing the boxplots in two is the decision threshold that corresponds to the red point on the associated ROC curve. FCD values below the threshold are true positives and those above the threshold are false negatives. Normal brain values below the threshold are false positives and those above the threshold are true negatives.

Table 5 Benchmark classification metrics for the future machine learning models

Spectral bins	**1172 cm^{-1}**	**1604 cm^{-1}**
Sensitivity	0.74	0.70
Specificity	0.66	0.64

As a benchmark for future machine learning algorithms, the classification performance should ensure that FCD samples are correctly identified at least 70% of the time, while normal brain samples should be accurately classified at least 64% of the time.

CHAPTER 5 CONCLUSION AND RECOMMENDATIONS

The aim of this project was to develop a cutting-edge system to assist surgeons in diagnosing FCD during surgical procedures. We were the first group in the world to ever attempt this.

Two key hypotheses have been formulated for this project:

1. *The enhancements made to the new Raman spectroscopy system will enable it to perform real-time measurements of FCD tissue during surgical interventions.*

2. *The improvements incorporated into the new Raman spectroscopy system will result in larger sensitivity and specificity for detecting FCD lesions compared to currently available imaging modalities.*

The developed Raman handheld point probe system takes acquisitions in ten times less time than the systems used in previous studies. Because each acquisition fills the dynamic range of the CCD camera in less than a second, by optimizing acquisition parameters it is possible to do real time Raman spectroscopy.

There were two limitations with the work presented in this Master's thesis: 1) the size of the dataset (number of patients, number of spectra/biopsies) was limited compared to previous studies from our lab (David, et al., 2023; Ember, et al., 2024), 2) the spectral quality of the spectroscopic data, measure by the quality factor (QF), was also relatively low. The clinical study that I initiated at the Children's Hospital and CHUSJ is currently underway with a fully optimized system and currently recruiting at the pace of approximately 1 patient every two weeks. The study will run for another 2 to 3 years, culminating with a target of at least 150 FCD patients. Further, on additional clinical site was recruited (CHU Québec) with a planned start data March 2025. In the meantime, two research areas could be explored to improve the acquisition process. As it relates to spectral quality, a new software module was developed by the laboratory optimizing QF live during acquisition which now allows spectral quality with QF > 0.6 to be attained, compared to an average value of QF =0.4 for the current study. This will be key to improving FCD detectability since we have demonstrated, in the current study, that the spectral changes between normal and FCD are, for example, more subtle than what was observed when detecting brain tumors using Raman spectroscopy (Leblond, et al., 2025; Ember, et al., 2024).

Despite the limited amount of data available and the relatively low quality of the spectra, we were able to establish minimal levels of sensitivity and specificity based on the detection of single Raman features. This established sensitivity and specificity of detection at ~70% using either the band at 1172 cm^{-1} or 1064 cm^{-1}. Despite low values, this is a powerful result because future developments will involve the development of machine learning models simultaneously exploiting a large number of bands providing complementary biomolecular information, based on a dataset that will have an improved spectral quality, i.e. a reduced level of stochastic noise.

Other aspects will need to be developed further. First, finding a way to mitigate all light background from scialytic lights, neon lights, screens and neuronavigational head so the acquisition process could more easily be integrated into the surgical one. Second, looking into using the CEM43 metric instead of the maximal permissive exposure of the skin and eyes as a safeguard parameter for the acquisitions. A recent article from the laboratory showed that the acquisition parameters could be more than doubled before being dangerous for the internal organs (Daoust, et al., 2023).

REFERENCES

Aaboubout, Y., Nunes Soares, M., Bakker Schut, T., Barroso, E., van der Wolf, M., Sokolova, E., . . . van Lanschot, C. (2023). Intraoperative assessment of resection margins by Raman spectroscopy to guide oral cancer surgery. *Analyst*, 148(17):4116-4126. doi:10.1039/d3an00650f

Askoro, R., Kagawa, K., Seyama, G., Okamura, A., Hashizume, A., Onari, T., . . . H. N. (2024). Prediction of Seizure Outcome Using Combinations of Four Noninvasive Presurgical Modalities in Magnetic Resonance Imaging-negative Focal Intractable Epilepsy. *Neurol Med Chir (Tokyo)*. doi:10.2176/jns-nmc.2024-0194

Ayalon, I., Friedman, S., Meidan, B., Sadot, E., Constantini, S., Uliel-Sibony, S., & Roth, J. (2024). Immediate postoperative course in the pediatric intensive care unit following epilepsy surgery. *Childs Nerv Syst*, 41(1). doi:10.1007/s00381-024-06681-5

Bruin, J. (2011, feb). *newtest: command to compute new test*. Récupéré sur UCLA: Statistical Consulting Group: https://stats.oarc.ucla.edu/stata/ado/analysis

Daoust, F., Tavera, H., Dallaire, F., Orsini, P., Savard, K., Bismuth, J., . . . Leblond, F. (2023). A clinical Raman spectroscopy imaging system and safety requirements for in situ intraoperative tissue characterization. *Analyst*, 148(9):1991-2001. doi:10.1039/d2an01946a.

David, S., Tran, T., Dallaire, F., Sheehy, G., Azzi, F., Trudel, D., . . . Meterissian, S. (2023). In situ Raman spectroscopy and machine learning unveil biomolecular alterations in breast cancer. *Journal of Biomedical Optics, 28*(3), 360009.

de Bie, K., van Kollenburg, R. .., L.A.M.J.G., v. R., Almasian, M., Freund, J., Bloemen, P., . . . de Bruin, D. (2024). Outcomes of CEM43 in Predicting Thermal Damage Induced by Focal Laser Ablation in Controlled Ex Vivo Experiments: A Comparison to Histology and MRI. *Lasers in Surgery and Medicine*, 56: 723-733. doi:https://doi.org/10.1002/lsm.23834

De Mazière, M., Sierens, C., & Schoemaker, D. (1989). Analysis of dephasing signal in picosecond stimulated-Raman-gain experiments. *Journal of the Optical Society of America B*, 6(12), 2376. doi:doi:10.1364/josab.6.002376

DePaoli, D., Lemoine, É., Ember, K., Parent, M., Prud'homme, M., Cantin, L., . . . Côté, D. (2020). Rise of Raman spectroscopy in neurosurgery: a review. *J Biomed Opt*, 25(5):1-36. doi:10.1117/1.JBO.25.5.050901

Desroches, J., Jermyn, M., Mok, K., Lemieux-Leduc, C., Mercier, J., Pichette, J., . . . Leblond, F. (2015). Characterization of a Raman spectroscopy probe system for intraoperative brain cancer tissue detection and classification. *Biomedical Optics Express, 6*(7), 2380-2397.

Desroches, J., Lemoine, É., Pinto, M., Marple, E., Urmey, K., Diaz, R., . . . Leblond, F. (2019). Development and first in-human use of a Raman spectroscopy guidance system integrated with a brain biopsy needle. *J Biophotonic*, 12(3). doi:10.1002/jbio.201800396.

Ember, K., Dallaire, F., Plante, A., Sheehy, G., Guiot, M.-C., Agarwal, R., . . . Petrecca, K. (2024). In Situ Brain Tumor Detection Using the Raman Spectroscopy Sentry System – Results of a Multicenter Study. *Scientific Reports*.

Fukutomi, D., Ishii, K., & Awazu, K. (2016). Determination of the scattering coefficient of biological tissue considering the wavelength and absorption dependence of the anisotropy factor. *Opt Rev*, 23, 291–298. doi:https://doi.org/10.1007/s10043-015-0161-y

Guerrini, R., & Barba, C. (2021). Focal cortical dysplasia: an update on diagnosis and treatment. *Expert Review of Neurotherapeutics*, 1–12. doi:doi:10.1080/14737175.2021.1915135

Huang, H., Shi, H., Feng, S., Chen, W., Yu, Y., Lin, D., & Chen, R. (2012). Confocal Raman spectroscopic analysis of the cytotoxic response to cisplatin in nasopharyngeal carcinoma cells. *Anal. Methods.*, 5. 260-266.

Jayalakshmi S, N. S. (2019). Focal Cortical Dysplasia and Refractory Epilepsy: Role of Multimodality Imaging and Outcome of Surgery. *AJNR Am J Neuroradiol.*, 40(5):892-898. doi:10.3174/ajnr.A6041.

Johansson, J. D. (2010). Spectroscopic method for determination of the absorption coefficient in brain tissue. *J. Biomed. opt.*, 15(5) 057005. doi:https://doi.org/10.1117/1.3495719

Leblond, F., Dallaire, F., Ember, K., Le Moël, A., Blanquez-Yeste, V., Tavera, H., . . . Petrecca, K. (2025). Quantitative assessment of the generalizability of a brain tumor Raman spectroscopy machine learning model to various tumor types including astrocytoma and oligodendroglioma. *J Biomed Opt*, 30(1):010501. doi:10.1117/1.JBO.30.1.010501

Lemoine, É., Dallaire, F. .., Yadav, R. .., Agarwal, R. .., Kadoury, S. .., Trudel, D. .., . . . Leblond, F. (2019). Feature engineering applied to intraoperative in vivo Raman spectroscopy sheds light on molecular processes in brain cancer: a retrospective study of 65 patients. *Analyst*, 144(22):6517-6532. doi:10.1039/c9an01144g

Lukina Maria, Y. K. (2021). Label-Free Macroscopic Fluorescence Lifetime Imaging of Brain Tumors. *Frontiers in Oncology*, 11. doi:10.3389/fonc.2021.666059

Lukina, M. &. (2016). Metabolic Imaging in the Study of Oncological Processes (Review). *Sovremennye tehnologii v medicine*, 8. 113-126. doi:10.17691/stm2016.8.4.16.

Moreno, M. &. (2020). In vivo near-infrared fluorescent optical imaging for CNS drug discovery. *Expert Opinion on Drug Discovery.*, 15. 1-13. doi:10.1080/17460441.2020.1759549.

Najm, I., Lal, D., Alonso Vanegas, M., Cendes, F., Lopes-Cendes, I., Palmini, A., . . . Garbelli, R. (2022). The ILAE consensus classification of focal cortical dysplasia: An update proposed by an ad hoc task force of the ILAE diagnostic methods commission. *Epilepsia, 63*(8), 1899-1919.

Neugebauer F, A. M. (2022). Validating EEG, MEG and Combined MEG and EEG Beamforming for an Estimation of the Epileptogenic Zone in Focal Cortical Dysplasia. *Brain Sci.*, 12(1). doi:doi: 10.3390/brainsci12010114.

Sandell, J. a. (2011). A review of in-vivo optical properties of human tissues and its impact on PDT. *J. Biophoton*, 4: 773-787. doi: https://doi.org/10.1002/jbio.201100062

Shakhatreh, L., Janmohamed, M., Baker, A. A., Willard, A., Laing, J., Rychkova, M., . . . Kwan, P. (2022). Interictal and seizure-onset EEG patterns in malformations of cortical development: A systematic review,. *Neurobiology of Disease*, 105863. doi:https://doi.org/10.1016/j.nbd.2022.105863.

Shapey, J., Xie, Y., Nabavi, E., Ebner, M., Saeed, S. R., Kitchen, N., . . . Vercauteren, T. J. (2022). Optical properties of human brain and tumour tissue: An ex vivo study spanning the visible

range to beyond the second near-infrared window. *, J. Biophotonics*, 15(4), e202100072. doi:https://doi.org/10.1002/jbio.202100072

Sheehy, G., Picot, F., Dallaire, F., Ember, K., Nguyen, T., Petrecca, K., . . . Leblond, F. (2023). Open-sourced Raman spectroscopy data processing package implementing a baseline removal algorithm validated from multiple datasets acquired in human tissue and biofluids. *Journal of biomedical optics, 28*(2).

Sowers, T., VanderLaan, D., A., K., Onohara, D., Schmarkey, S., Rousselle, S., . . . Emelianov, S. (2022). In vivo safety study using radiation at wavelengths and dosages relevant to intravascular imaging. *J Biomed Opt.*, (1):016003.

Spitzer, H., Ripart, M., Whitaker, K., D'Arco, F., Mankad, K., Chen, A., . . . Davies, S. (2022). Interpretable surface-based detection of focal cortical dysplasias: a Multi-centre Epilepsy Lesion Detection study. *Brain*, 145(11):3859-3871. doi:10.1093/brain/awac224

Teich, B. E., & Saleh, M. C. (2019). *Fundamentals of photonics, Third edition.* (N. Wiley, Éd.) Hoboken,: Wiley series in pure and applied optics.

Trang, T., Leblond, F., Dallaire, F., Cayrol, R., & Dudley, R. (in press). Single-cell Raman spectroscopy detects pediatric focal cortical dysplasia. *Epilepsia*.

Tuschel, D. (2021). Peak Shape and Closely Spaced Peak Convolution in Raman Spectra. *Spectroscopy*, 36(9), 10-14. doi:https://doi.org/10.56530/spectroscopy.ba4682f3

West, S., Nevitt, S., Cotton, J., Gandhi, S., Weston, J., Sudan, A., . . . Newton, R. (2019). Surgery for epilepsy. *Cochrane Database Syst Rev*, 6(6):CD010541. doi:10.1002/14651858.CD010541.pub3.

Yang, S. (2022). 6. High-Wavenumber Raman Analysis. Dans S. e. Yang, *Recent Developments in Atomic Force Microscopy and Raman Spectroscopy for Materials Characterization.* IntechOpen.

Yao, L., Cheng, N., Chen, A., Wang, X., Gao, M., Kong, Q., & Y., K. (2024). Advances in Neuroimaging and Multiple Post-Processing Techniques for Epileptogenic Zone Detection of Drug-Resistant Epilepsy. *J Magn Reson Imaging*, 60(6):2309-2331. doi:10.1002/jmri.29157

Yuan, X., & Mayanovic, R. (2017). An Empirical Study on Raman Peak Fitting and Its Application to Raman Quantitative Research. *Appl Spectrosc*, 71(10):2325-2338. doi:10.1177/0003702817721527